Available online at www.sciencedirect.com
ScienceDirect
International Journal of Heat and Fluid Flow 29 (2008) 449–459
International Journal of HEAT AND FLUID FLOW
www.elsevier.com/locate/ijhff

Simulation and measurement of 3D shear-driven thin liquid film flow in a duct

H. Lan, M. Friedrich, B.F. Armaly *, J.A. Drallmeier

Department of Mechanical and Aerospace Engineering, University of Missouri – Rolla, Rolla, MO 65401, United States

Received 2 May 2007; received in revised form 9 November 2007; accepted 16 December 2007
Available online 31 January 2008

Abstract

Three-dimensional flow behavior of thin liquid film that is shear-driven by turbulent air flow in a duct is measured and simulated. Its film thickness and width are reported as a function of air velocity, liquid flow rate, surface tension coefficient, and wall contact angle. The numerical component of this study is aimed at exploring and assessing the suitability of utilizing the FLUENT-CFD code and its existing components, i.e. Volume of Fluid model (VOF) along with selected turbulence model, for simulating the behavior of 3D shear-driven liquid film flow, through a comparison with measured results. The thickness and width of the shear-driven liquid film are measured using an interferometric technique that makes use of the phase shift between the reflections of incident light from the top and bottom surfaces of the thin liquid film. Such measurements are quite challenging due to the dynamic interfacial instabilities that develop in this flow. The results reveal that higher air flow velocity decreases the liquid film thickness but increases its width, while higher liquid flow rate increases both its thickness and width. Simulated results provide good estimates of the measured values, and reveal the need for considering a dynamic rather than a static wall contact angle in the model for improving the comparison with measured values.

Keywords: Thin film; Measurements; VOF model; Shear-driven film

1. Introduction

Thin liquid films (with thickness in an order of 100 μm) that are shear-driven by turbulent air flow in a duct develop in many engineering applications that are associated with film breakup and atomization. Such films breakup/atomize as they encounter sudden expansion in geometry as is the cases in fuel and air mixture preparation for spark ignition engines and atomizers (Samenfink et al., 1999). The average film characteristics, such as its thickness and velocity, prior to its atomization, influence significantly the atomization/breakup process (Samenfink et al., 1999). Numerous publications have appeared in the literature on this general topic (Samenfink et al., 1999; Wang et al., 2004; Friedrich et al., 2006,; Wittig and Himmelsbach, 1992). Specifically, Wittig and Himmelsbach (1992) reported some measured results for 2D shear-driven thin liquid film in a duct and proposed an "equivalent rough wall" model for simulating its flow. The results from this model compared favorably with measured values (Wittig and Himmelsbach, 1992), but its applicability is limited to only 2D flow and it cannot be extended to separated flow. To the authors' knowledge, a coordinated effort of measuring and simulating the 3D flow behavior of shear-driven thin liquid film has not appeared in the literature and that motivated the present study.

2. Experimental facilities

The experimental tunnel that is used for examining the 3D flow behavior of shear-driven liquid film is shown in Fig. 1, and the optical system that is used to measure the film thickness is shown in Fig. 2. The tunnel has a rectangular test section with a height of 0.0203 m and width of 0.1016 m (i.e. an aspect ratio of approx. 5), and has an

* Corresponding author. Tel.: +1 573 341 4601; fax: +1 573 341 4607.
E-mail address: armaly@umr.edu (B.F. Armaly).

0142-727X/$ - see front matter © 2007 Elsevier Inc. All rights reserved.
doi:10.1016/j.ijheatfluidflow.2007.12.003

Nomenclature

h_f	film thickness
v	kinematic viscosity
Re_f	film Reynolds number $Re_f = u_f h_f / v$ (By approximation $\dot{V}_f = u_f h_f W_f) = \dot{V}_f/(W_f v)$
u_f	average film velocity
U_g	average velocity of gas flow
$\dot{V}_f$	liquid flow rate
W_f	film width
X	streamwise coordinate
Y	transverse coordinate
Z	spanwise coordinate

Greek symbols

α	volume fraction
θ_w	contact angle (or wall contact angle)
$\theta_{w,S}$	static wall contact angle
$\theta_{w,D}$	dynamic wall contact angle
σ	surface tension coefficient

Subscripts

f	film (liquid phase)
g	gas (gas phase)
w	wall

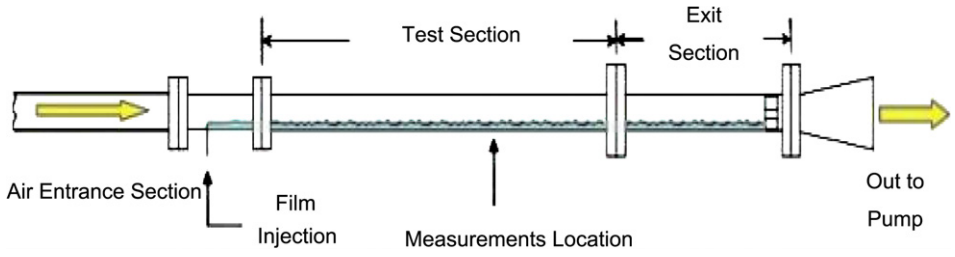

Fig. 1. Schematic of experimental tunnel.

aluminum frame with glass windows on both sides and upper wall for flow visualization and optical measurements. The inlet section of the tunnel is 1.43 m in length and has an inlet nozzle for smooth transition of the air flow into the tunnel. It is sufficiently long to provide fully developed turbulent air flow at the inlet of the test section where the liquid film is injected into the air stream. The combined length of the test and the exit sections of the tunnel is 0.5 m long. The exit section of the tunnel provides for a transition from rectangular duct to a 0.102 m diameter pipe that is connected to a liquid ring vacuum pump that pulls the air through the tunnel, and is capable of generating average air velocity of up to 45 m/s through the tunnel's test section. The volumetric air flow rate is measured by a laminar flow element (corrections are made for local temperature and pressure resulting in an uncertainty of <3%) and that is used to deduce the average air velocity inside the test section of the tunnel. The liquid film is injected into the air flow through a porous media that is placed in the spanwise center of the bottom wall of the test section, and has an injection width that is equal to 3/4 of the full width of the test section (or 0.0762 m wide). The liquid volumetric flow rate is measured by a rotometer with an uncertainty of 2.5%. Optical measurements of the shear-driven liquid film thickness and width are made at a location that is 0.225 m downstream from the end of film injection region. The injected liquid film is water with 0.1% mass concentration of surfactant (Surfynol 465) resulting in a fluid with a surface tension coefficient of 0.042 N/m (Wang et al., 2004). The addition of the surfactant to the water is needed during the experiment in order to develop a uniform liquid film layer on the bottom surface of the tunnel's test section.

An interferometric technique for measuring the thickness of a stationary thin liquid film, shown schematically in Fig. 2, was initially developed by Ohyama et al. (1988) and improved by Nosoko et al. (1996) and by Kelly-Zion et al. (2004) who measured the film thickness of an evaporating (non-flowing and smooth) liquid film. The use of this technique is extended in this study for measuring the local dynamic thickness of shear-driven liquid film having rough (rippled) interface. The technique makes use of the phase shift between the reflections of incident light from the top and bottom surfaces of the liquid film. When the light beam approaches the liquid film with a certain incident angle, a series of bright and dark fringes are formed. The number of these fringes which occur in a specified field of view in the reflected beam is used to determine the instantaneous film thickness. The field of view is defined by the aperture that is used in the receiving optics. The spatial resolution is determined based on the spot size of the incident light beam, which is approximately 10 μm for the current configuration of the transmitting optics. Temporal resolution is determined by the rate at which the fringe imaging is taking place. For the results shown in this study, a high frame-rate camera, a Photron 1280 PCI, operating at 2000 frames per second is used which results in an exposure time of 0.5 ms for the chosen shutter setting.

The optical configuration of the film thickness measurement system is shown in Fig. 2a. A 10 mW Helium–Neon laser is collimated to approximately a 0.02 m diameter. A

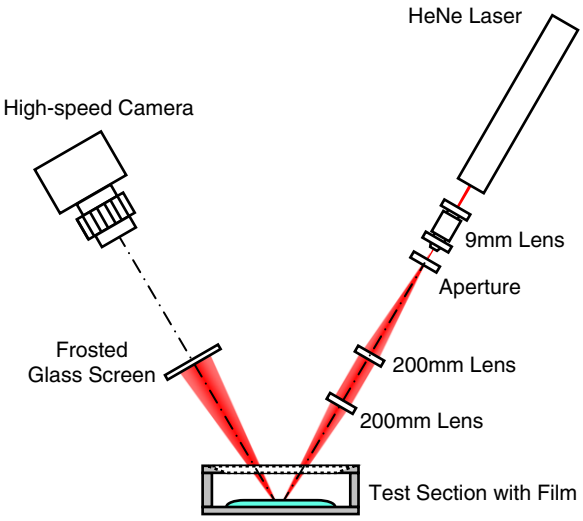

Fig. 2a. Schematic of the interferometric film thickness measurement system.

0.1 m focal length lens is used to develop a spot size of less than 10 μm diameter on the surface of the film. The light reflected from the film, which forms the interference pattern, is imaged on a diffusing glass plate. As shown in Fig. 2b, when the light approaches the film over a small range of incident angles, a portion of the incident light reflects at the top surface of the liquid film and a portion transmits through the film and reflects at the bottom surface. The refraction of light in the film causes the light leaving the film to interfere either constructively or destructively, depending on whether the change causes the light waves to be in phase or out of phase. For one light ray incident on the film at an angle θ_i, the phase difference, δ, is calculated to be

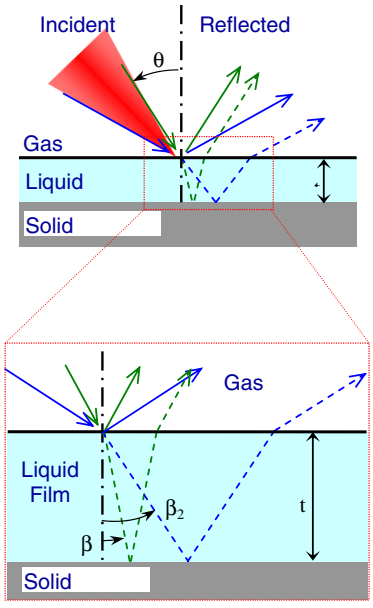

Fig. 2b. Schematic of the reflection and refraction of the laser beam.

$$\delta = \frac{4\pi t}{\lambda_0}\left(n_l^2 - n_g^2 \sin^2\theta_i\right)^{1/2} \pm \pi \tag{1}$$

where t is the film thickness, λ_0, is the wavelength of light beam, and n_l and n_g are the indices of refraction of the liquid film and gas, respectively.

For light that is incident over a range of angles as shown in Fig. 2b, a series of light and dark fringes appear in the reflected light in the shape of concentric arcs. Nosoko et al. (1996) developed the following equations to compute the film thickness from a measurement of the number of fringes, F

$$t = \frac{\lambda_0 F}{2n_l(\cos\beta_1 - \cos\beta_2)} \tag{2}$$

where β, the angle of refraction, is defined by Snell's law as

$$\sin\beta = \frac{\sin\theta_i}{n_l} \tag{3}$$

Therefore, the number of these fringes which occur in a specified field of view is used to determine the film thickness.

An uncertainty analysis of the film thickness measurement by this optical system was performed for the current configuration. The largest system uncertainties were in the incident beam angle, the distance between the film and the measuring screen, the field of view on the screen, and the number of fringes in a given frame. Of these, the uncertainty in the incident beam angle was determined to have the largest impact on the final results. An incident beam angle of $31° \pm 1°$ from the vertical was chosen to facilitate entrance into the test section while reducing the sensitivity of the measured film thickness to the incident beam angle. A total systematic uncertainty based on these considerations was $\pm 5\%$ of the measured value. Additionally, a validation experiment was performed using a sapphire disk of known thickness and smooth interface, whose measured fringes are shown in Fig. 3. The measurement of a nominal

Fig. 3. Fringe pattern of the interferometric technique – validation with a sapphire disk.

508 μm thick sapphire disk was within the manufacturers' uncertainty of 10%. More details on the development of this interferometric measurement technique for measuring the dynamic liquid film thickness can be found in Friedrich et al. (2007).

The surface of the shear-driven liquid film is found to be rippled as it is driven downstream by the turbulent air flow due to the formation of Kelvin–Helmholtz instabilities. It is important to note that this interferometric technique will only display fringes on the diffusing glass plate for film surfaces that are nearly parallel with the bottom surface of the test section. Hence, dynamic film thickness measurements will only be recorded at wave peaks and wave valleys rather than continuously. A typical result of a measured dynamic liquid film thickness at the spanwise center of the tunnel by this method is shown in Fig. 4. The erratic behavior in the reported instantaneous liquid film thickness measurements is due to the instabilities (ripples) that develop on the film surface and the nature of the measurement technique which provides results only for wave peaks and valleys that appear on the surface of the shear-driven liquid film. Each point thickness measurements is produced from one fringe pattern imaged at 2000 frames per second, but with approximately only 200 frames that are producing fringes within the image acquisition period of one second. The background noise content of those selected images that are taken during the actual film thickness measurements is significant. To improve the accuracy of extracting meaningful data from these images and to reduce the data reduction time of such a process, an automated Fast Fourier Transform (FFT) technique is developed for identifying the image frames with valid fringes as well as for determining the fringe spacing in these selected images, along with calculating the corresponding film thickness resulting from that selected image as shown in Fig. 4. The horizontal line in that figure represents the mean thickness, averaged over the time, resulting from all the selected frames for that run. It is important to note here that only the mean thickness and width of the liquid film are of interest in this study.

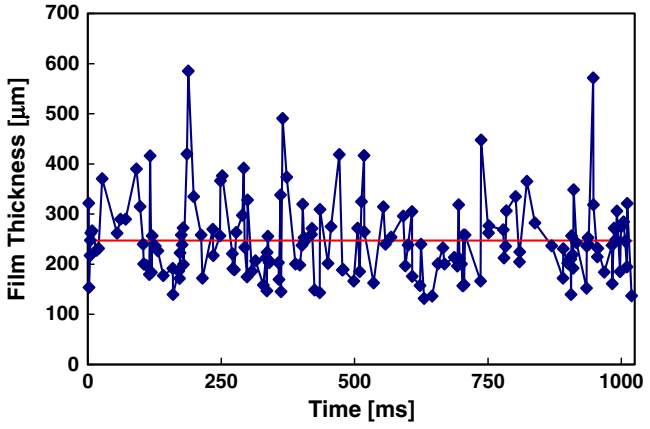

Fig. 4. Time series of measured film thickness ($U_g = 30$ m/s, $\dot{V}_f = 13.01$ cm^3/s).

Fig. 5. Static wall contact angle measurement for water with surfactant ($\sigma = 0.042$ N/m).

Hence only an average behavior for the film thickness is determined from the distribution of thicknesses obtained over a sufficiently long time interval (~2 s) over which the mean stabilized.

Two methods are employed to measure the liquid film width. The first is to traverse the focus of a Helium–Neon laser across the surface of the film and note the change in reflectivity at the edge of the film. The second is by a mechanical means where a digital caliper is used and viewed through the top access window of the test section. Both methods produced similar results with an uncertainty of less than ±3 mm. It should become clear from the above discussion of the experimental technique that the measurement of the liquid film width is rather simple and more robust than the measurements of the film thickness (its uncertainty is significantly smaller). The dynamic instabilities that develop at the film interface make the film thickness measurements very challenging and add significant level of uncertainty to the measured results.

Measurement of the static wall contact angle is made using a static drop of water-surfactant solution on a solid surface which is of the same material and surface finish as that used to construct the bottom wall of the test section, and a photomicroscope is used to observe the wall contact line between the liquid drop and the solid substrate. Multiple measurements (typically 24) were made of the wall contact angle resulting in an uncertainty of 3° based upon measurement repeatability. A static wall contact angle of 30° was measured for liquid that has a surface tensions coefficient of 0.042 N/m (water with 0.1% volume concentration of surfactant), and a view of the liquid drop and the wall contact angle that was measured is shown in Fig. 5. Measurements of the static wall contact angle were repeated using different drop volumes to determine an average value and to establish the uncertainty in such measurement.

3. Simulation procedure

The suitability of utilizing the Volume of Fluid model (VOF) that is a component of the FLUENT-CFD code for simulating three-dimensional shear-driven thin liquid film flow behavior in a duct is assessed by a comparison between measured and simulated film thickness and width as a function of both air and liquid flow rates. A schematic of the computational domain that describes the experimental geometry and flow conditions that were discussed in the

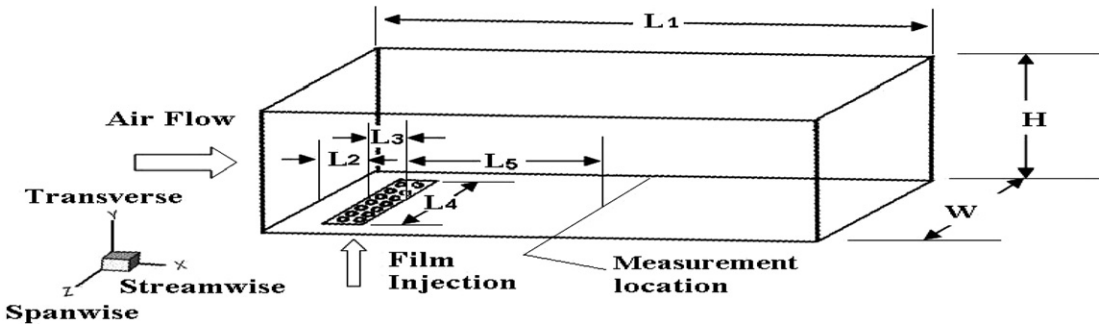

Fig. 6. Schematic of the computational domain.

previous section of this paper is shown in Fig. 6. The height H, the width W, and the length L_1 of the computational domain are 0.0203 m, 0.1016 m, and 0.6 m, respectively. Air flow is introduced at the inlet plane ($X = 0$ m), and liquid is injected through a porous region in the bottom wall of the duct between $X = L_2 = 0.0127$ m and $X = L_2 + L_3 = 0.0254$ m. The developing interfacial shear force drives the injected liquid in the direction of the air flow, resulting in a thin liquid film flow adjacent to the bottom wall of the duct. The width of the liquid injection region is $L_4 = 0.0762$ m and it is 3/4 of the duct's width. Measurements of film thickness and width are performed at a location that is 0.225 m downstream from the end of the film injection region (at $X = 0.25$ m) and the simulated results at that location are compared with these measurements.

The length of the computational domain was selected as $L_1 = 0.6$ m based on the fact that the use of a larger length (i.e. of 1.0 m) resulted in less than 2% change in the predicted film thickness at the measuring location of $X = 0.25$ m. Due to geometric and flow symmetry for both the air and the liquid film flow relative to the center plane of the duct, only half of the duct's width (with half width as 0.0508 m) is used in the simulation, and symmetry boundary condition is imposed at the spanwise center plane of the duct. The no-slip boundary condition is imposed on all of the bounding walls. Fully developed turbulent air flow is used as the inlet boundary conditions, and that was generated by using a separate 3D simulation of a single phase turbulent air flow in a duct having the same dimensions as the experimental/simulated duct. A uniform transverse velocity (normal to the air flow) is specified at the liquid injection region (at the bottom wall of the duct), which is calculated from the selected liquid flow rate (experimentally measured) and the area of the liquid injection region. Pressure outlet boundary condition is used at the exit plane of the computational domain. Isothermal flow conditions are considered and properties are evaluated at a temperature of 20 °C.

The VOF model is an interface-tracking technique for multiphase flow that is applied to a fixed Eulerian mesh and has the capabilities of determining the volume fraction of each phase in every computational cell, and utilizing that information to locate approximately the position of the interface between phases. A single set of momentum and turbulent transport equations are shared by the two phases (liquid film and air), and this two-phase flow is treated as quasi-single phase flow with variable properties. These properties, like density and viscosity, vary with position and are a function of the individual properties of the two phases weighted by the liquid volume fraction in each computational cell. The volume fraction of the liquid phase in each computational cell is tracked throughout the computational domain and it can vary between zero and unity. The volume fraction of the gas phase in each computational cell equals to unity minus the volume fraction of the liquid phase in that cell. The interface position, as determined from this simulation, identifies the boundary of the liquid film (indicating film thickness and width).

The calculation of the surface tension force is dependent on the gradient of the liquid volume fraction and the surface tension coefficient (σ) with a direction that is normal to the liquid film surface. For the near wall interfacial cells the surface of the film is affected by the wall contact angle (θ_w), i.e. wall adhesion effects (Fluent Inc., 2004), and that influences the direction of the surface tension force in that region. Detailed description of the VOF model and the governing equations for velocity; volume fraction; and the varying properties, along with the solution procedure can be found in the FLUENT manual (Fluent Inc., 2004). Low-Reynolds k–ε turbulence model (AKN) (Abe et al., 1994) is used to simulate the turbulence in the flow. The SIMPLE algorithm is used to deal with the coupling computations between the flow field and the pressure field (Tao, 2001).

For the conditions that are considered in this study, the liquid film thickness is always less than 1000 μm (1 mm), and for that reason very small cell size is used in this region to insure that a sufficient number of grid points are located inside the very thin liquid film and the interface region. Non-uniform mesh is used in the simulation with finer mesh inside the liquid film and in the interface region. The smallest mesh size is placed in the interface region (of $200 < Y < 800$ μm) in order to identify more accurately the interface between the liquid and the air. Different sizes and distributions of mesh were examined and their results were compared in order to identify the one that generates a grid independent solution. A grid with approximately 0.7 million points ($X \times Y \times Z$ as $98 \times 110 \times 62$), with 40

Table 1
Grid independence study

Mesh ($X \times Y \times Z$)	Parameter	
	Film thickness (μm)	Film width (mm)
98 × 90 × 62	271	65.3
98 × 100 × 62	288	65.7
98 × 110 × 62	285	66.0
98 × 110 × 52	285	64.8
98 × 120 × 72	283	66.2

of the transverse grid points located in the region of $Y < 500$ μm, is selected for generating the results that are presented in this study. The use of a mesh with a higher number of grid points (i.e. $X \times Y \times Z$ as 98 × 120 × 72) produced a less than 2% change in a film thickness and less than 1% change in the film width. Results from a grid independence study are reported in Table 1 for a case of air flow velocity equal to 30 m/s and film flow rate equal to 19.76 cm^3/s (surface tension coefficient $\sigma = 0.042$ N/m and wall contact angle $\theta_w = 30°$).

The simulation is performed using parallel computation on a cluster of personal computers. For one case, four (4) cluster nodes are used in parallel computation and each node has 1.96 GB of memory, and 2 CPU processors with 3.12 GHz clock speed. Typically 100 CPU hours is needed to get a converged solution. Under-relaxation factors are used with all the variables for better numerical stability. Due to the large difference in the properties of the two fluids, the relaxation factors for the density and body force are chosen as 0.6, and the relaxation factors for velocities and volume fraction are chosen as 0.5. A converged solution is achieved when the volume fraction residual is less than 10^{-6}. Different discretization schemes are used for different equations, i.e. for the pressure correction equation, a body force weighted scheme is used, and second order upwind scheme is applied to all the other equations.

4. Results and discussion

4.1. Interface criterion

An important issue that needs to be resolved when using the VOF model for simulating shear-driven liquid film is the manner by which the interface between the liquid and the gas is identified. When the differences in properties between the two phases are significant as is the case this study (around 1000 times difference in density and 100 times difference in viscosity for water and air), the transition region where the liquid volume fraction changes from 0 to 1 is relatively large and it can be as thick as hundreds of microns. Thus, it is very critical to select a meaningful criterion to determine the interface between the liquid film and the air based on contour lines of liquid volume fraction. In order to develop some logic for establishing such a criterion, the fraction of the injected liquid mass flow rate that is captured between the contour line of a selected

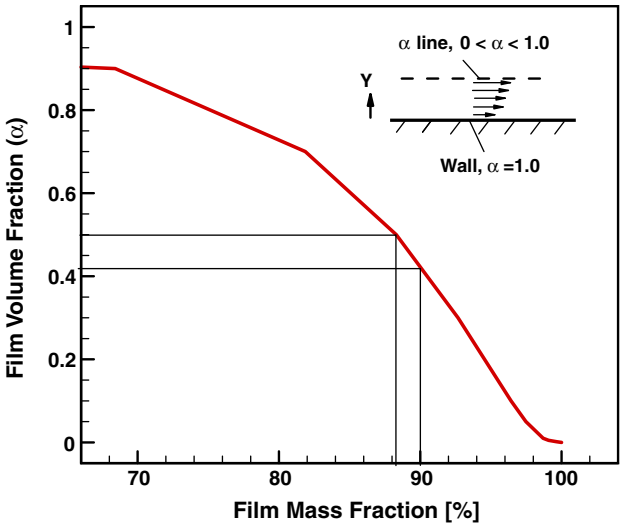

Fig. 7. Fraction of injected liquid film captured by a selected interface criterion (at $X = 0.25$ m).

liquid volume fraction and the bottom solid wall is calculated at the measuring station of $X = 0.25$ m, and the results are presented as a function of the liquid volume fraction in Fig. 7. The results in the figure show that 88% of the injected liquid film mass flow rate is captured if the interface is placed at a liquid volume fraction line of $\alpha_f = 0.5$, and similarly 90% of the injected liquid film mass flow rate is captured if the interface is placed at a liquid volume fraction line of $\alpha_f = 0.4$, i.e. 20% decrease in α_f results in only 2% increase in the captured injected liquid film mass flow rate. These results led to a selection of an interface criterion that places the liquid film interface at the contour line where the liquid volume fraction is equal to 0.5. The selection of a lower value for this criterion will result in larger liquid film thickness and width and the reverse will result from the selection of a higher value for this criterion.

The general average features of the simulated shear-driven thin liquid film are presented in Figs. 8–10. These

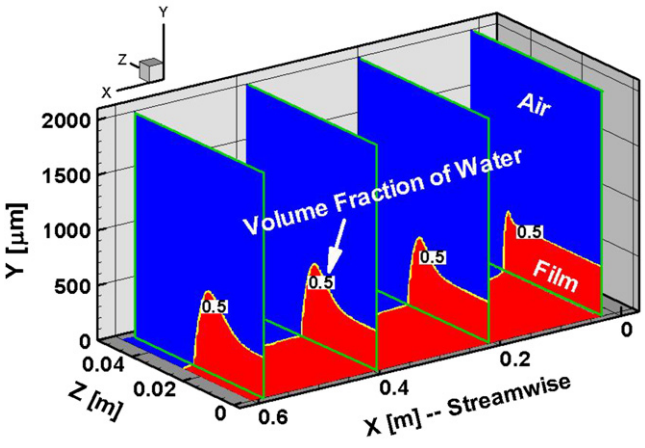

Fig. 8. General flow features of shear-driven liquid film (half width).

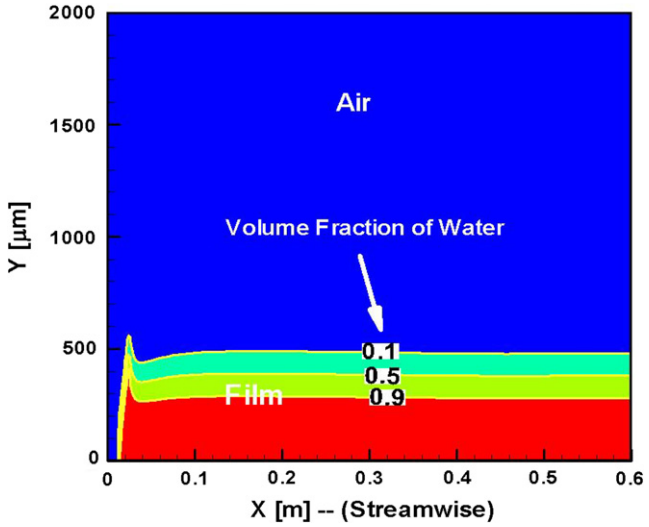

Fig. 9. Streamwise distribution of film thickness (at $Z = 0.0$).

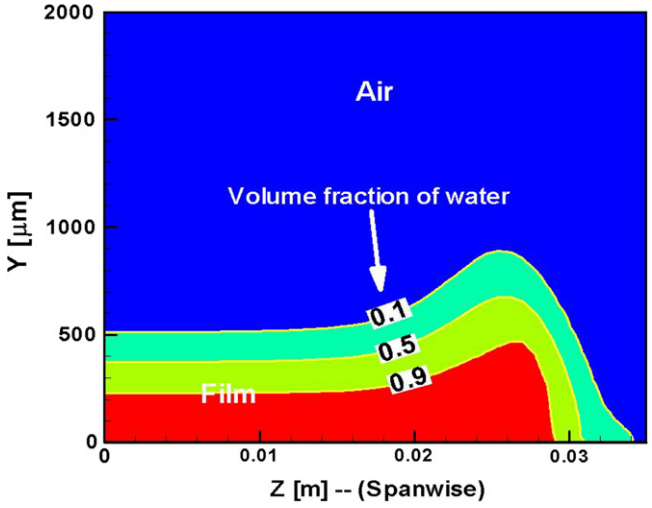

Fig. 10. Spanwise distribution of film thickness (at $X = 0.25$ m).

results are generated for air flow velocity of $U_g = 20$ m/s and film flow rate of $\dot{V}_f = 19.76$ cm^3/s ($\sigma = 0.042$ N/m, $\theta_w = 30°$). The spanwise distributions of the liquid film thickness at different streamwise locations are presented in Fig. 8. The film thickness at the liquid injection region is uniform in the spanwise direction, but a peak starts to develop at the outer edge of the liquid film (in the spanwise direction) quickly after its injection due to the effect of surface tension force. The streamwise distribution of the film thickness at the spanwise center plane of the duct ($Z = 0$) is presented in Fig. 9. A peak in the film thickness develops at the liquid injection region due to the transverse velocity component that is used to inject the liquid film into the air flow. That peak reduces rapidly after the injection region, and the flow reaches a steady thickness before the measuring location of $X = 0.25$ m, i.e. constant film thickness develops after $X = 0.15$ m. The simulated spanwise distribution of the film thickness at the measuring location in the test section, at $X = 0.25$ m, is presented in Fig. 10. Contour lines for different liquid volume fraction are shown in Figs. 9 and 10 to illustrate the effect of selecting different interface criterion on the film characteristics.

4.2. Changes due to air velocity and liquid flow rate

The results in Figs. 11 and 12 illustrate the influence of the average air velocity and liquid flow rate on the film thickness and width at the measuring location of $X = 0.25$ m. The liquid film thickness decreases but its width increases with increasing average air velocity for a fixed liquid flow rate as shown in Fig. 11. The higher average air velocity results in a higher interfacial shear stress that produces a higher liquid film velocity, thus causing

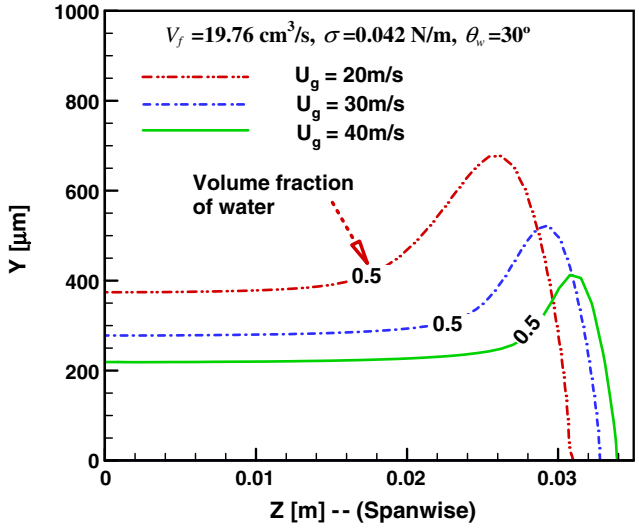

Fig. 11. Effect of air velocities on film thickness and width (at $X = 0.25$ m).

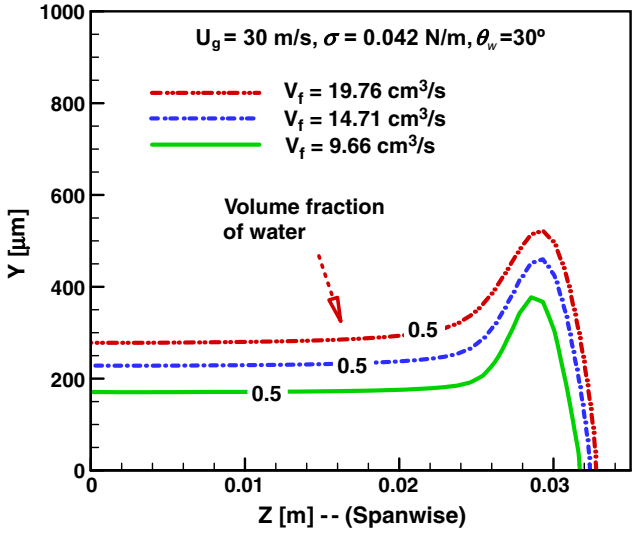

Fig. 12. Effect of liquid flow rate on film thickness and width (at $X = 0.25$ m).

the film thickness to decrease and its width to increase. The results in Fig. 12 illustrate that both the liquid film thickness and its width increase as the liquid flow rate increases for a fixed average air velocity. The effect of the liquid flow rate on the film thickness is more pronounced than its effect on the film width.

4.3. Changes due to surface tension

The surface tension force is dependent on the surface tension coefficient and the wall contact angle. The effect of surface tension coefficient (for a fixed wall contact angle), and the effect of wall contact angle (for a fixed surface tension coefficient) on the liquid film width is presented in Figs. 13 and 14, respectively. The results in these figures are for an average air velocity of $U_g = 30$ m/s and a liquid flow rate of $\dot{V}_f = 19.76$ cm^3/s, and they represent the streamwise distribution of the liquid film width. The width of the liquid film injection region, the center width line of the duct, and the outer wall boundary of the duct are shown in these figures for comparison. The results show that the width of the shear-driven liquid film can either decrease or slightly increase along the streamwise direction depending on the surface tension coefficient or the wall contact angle. At a fixed streamwise location, the liquid film width decreases if either the surface tension coefficient or the wall contact angle increases. The results in Fig. 13 for the case of surface tension coefficient of 0.014 N/m and a wall contact angle of 30°, and the results in Fig. 14 for the case of a surface tension coefficient of 0.042 N/m and wall contact angle of 15°, show nearly constant liquid film width in the streamwise direction. The effect of the surface tension force can be eliminated in the simulation by setting the magnitude of either the wall contact angle or the surface tension coefficient to be zero. The

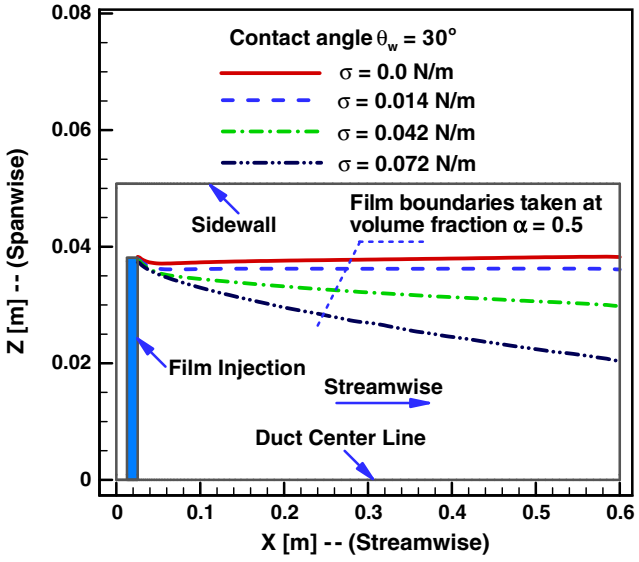

Fig. 13. Effect of surface tension coefficient on film width ($U_g = 30$ m/s, $\dot{V}_f = 19.76$ cm^3/s).

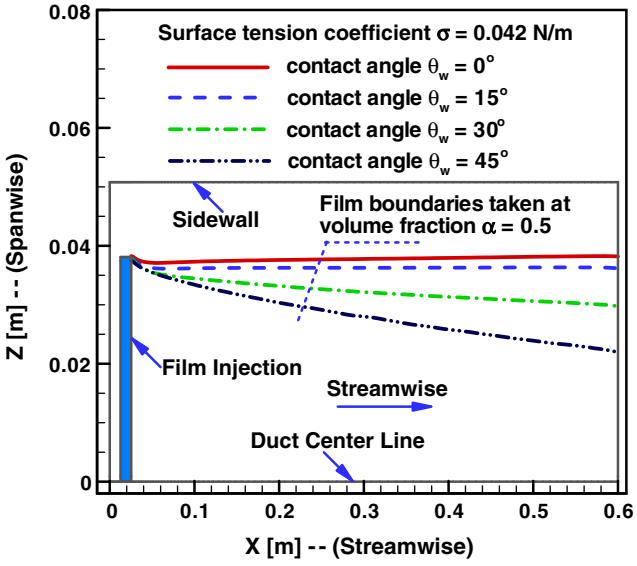

Fig. 14. Effect of wall contact angle on film width ($U_g = 30$ m/s, $\dot{V}_f = 19.76$ cm^3/s).

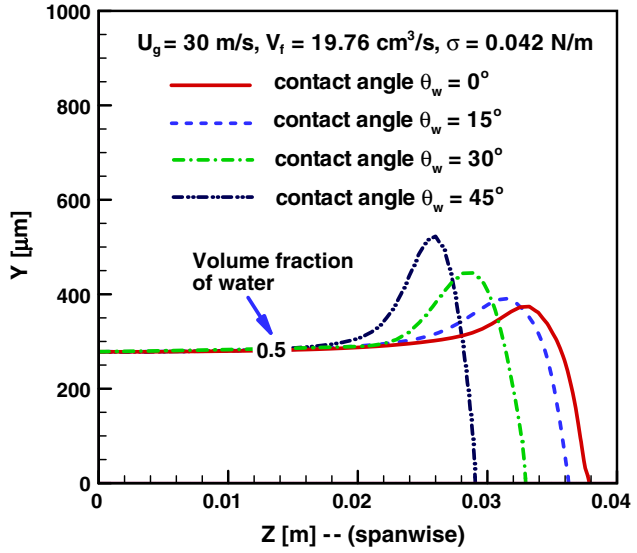

Fig. 15. Effect of wall contact angle on film thickness and width (at $X = 0.25$ m).

simulation results reveal that the film thickness at the center width of the duct at the measuring location of $X = 0.25$ m is not affected significantly by the surface tension force for the range of parameters that are considered in this study as can be seen in Fig. 15. The results in that figure show that the film width increases but its thickness at the center of the duct remains constant as the wall contact angle decreases at the measuring location of $X = 0.25$ m.

4.4. Comparison with measurements

Measurements of the liquid film thickness and width have been made using the facilities described in the previ-

ous section of this paper. The film thickness was measured only at the spanwise center of the duct at the measuring location of $X = 0.25$ m. Multiple measurements were performed for the same flow conditions in order to determine the repeatability and the standard deviation for these measurements. The standard deviation of the measured film thickness was determined to be 50 μm and that of the film width was 4.8 mm. The relatively large standard deviation for the film thickness is due to the significant film surface instabilities (ripples) that develop in this flow and the nature of the measuring technique (acquiring data only at the peaks and valleys of the dynamic film surface). Measurements are presented for two average gas velocities of 30 and 40 m/s, and for several liquid flow rates. Results for liquid film thickness are presented in Fig. 16, and results for liquid film width are presented in Fig. 17 along with the standard deviation (as error bars) for each of these measurements.

Uncertainties associated with the VOF simulation model could be attributed to the manner by which the surface tension force is modeled and to the fact that the steady state model is not capable of capturing the interfacial instabilities (ripples) that are observed experimentally and also due to not accounting for the dynamic nature of the wall contact angle. Additional uncertainty could be attributed to the manner by which film thickness and width are determined from the simulated results, i.e. interface criterion chosen as $\alpha = 0.5$. However, choosing different "α" values as an interface criteria can result in either higher or lower magnitude in film thickness and width, but it does not change significantly the slope of the simulated results. The results in Figs. 16 and 17 shows that simulated film thickness and width increase at a faster rate than measured values as a function of the liquid flow rate. But considering the difficulties and the uncertainties in both measurements

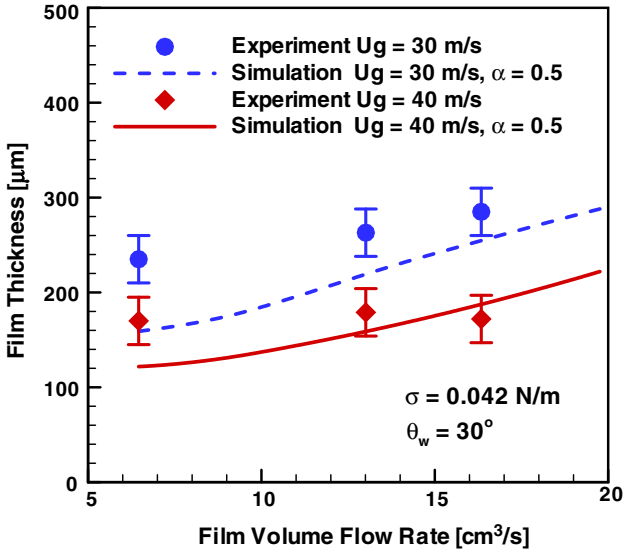

Fig. 16. Comparison between measured and predicted results for film thickness.

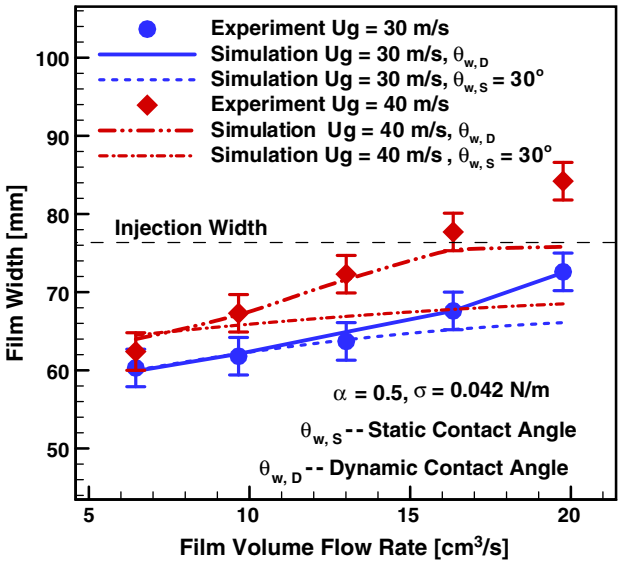

Fig. 17. Comparison of measured and predicted results for film width.

and simulations, the relatively reasonable comparison between simulated and measured results is actually quite encouraging and further improvements to the measuring technique might improve that comparison.

The film width results that are presented in Fig. 17 show that the use of a constant wall contact angle (the static wall contact angle of 30°) in the simulation does not yield the measured trend in the results as a function of liquid flow rate, particularly at high air and liquid flow rates. The use of a dynamic wall contact angle is explored (by using a different wall contact angle value for different flow conditions) as a mean of improving the comparison between predicted and measured results. Measuring or predicting the dynamic wall contact angle for different flow conditions is beyond the scope of this study, but since the measurements of the liquid film width is relatively simple and robust it was selected as the target (true value), and simulations were used to determine the magnitude of the wall contact angle that yielded the best comparison with measured values. The dynamic wall contact angles that were determined by such a process for the various flow conditions are tabulated in Table 2 (the film width and film Reynolds number values in the table were obtained from measured data), and the simulated results for the film width

Table 2
Dynamic wall contact angle variation (static wall contact angle $\theta_{w,S} = 30°$)

U_g (m/s)	Misc.	$\dot{V}_f$ (cm^3/s)				
		6.46	9.66	13.01	16.34	19.76
30	W_f (mm)	60.3	61.8	63.7	67.6	72.6
	Re_f	107	156	204	242	272
	$\theta_{w,D}$	30°	30°	28°	25°	16°
40	W_f (mm)	62.4	67.3	72.3	77.7	84.2
	Re_f	104	144	180	210	235
	$\theta_{w,D}$	30°	28°	19°	5°	0°

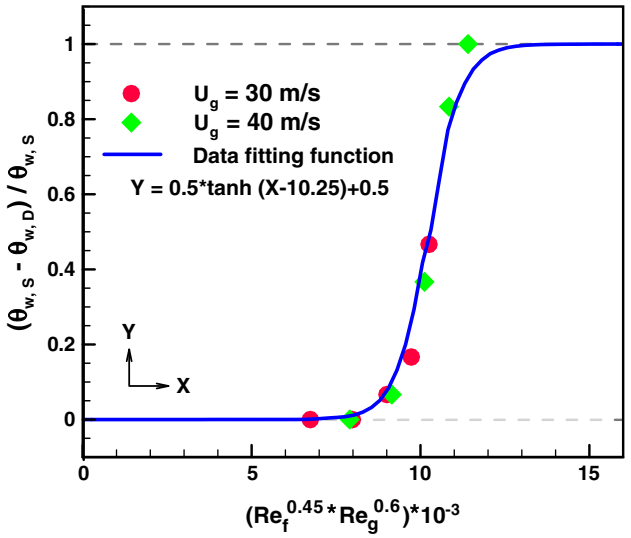

Fig. 18. Dynamic wall contact angle in shear-driven liquid film.

using these dynamic wall contact angles are presented in Fig. 17. With the exception of one measured point at the highest air and liquid flow rates (at air velocity of 40 m/s and liquid flow rate of 19.76 cm^3/s), the simulated results could be forced to agree with measured values by the proper selection of a dynamic wall contact angle. At the highest air and liquid flow rates significant level of instabilities and liquid breakup develop on the film surface and the liquid film spreads wider than the width of the liquid injection region (at the measuring location) moving very close to the sidewall of the duct. Since the simulation does not capture any of these surface instabilities it cannot be expected to compare well with measurements at high air and liquid flow rates. At these high flow rates, the use of a dynamic wall contact of zero in the simulation does not bring the simulated results closer to the measured values.

An attempt to correlate the dynamic wall contact angles that resulted from the above effort (tabulated in Table 2) with flow parameter is shown in Fig. 18. The figure shows that the dynamic wall contact angle is equal to the static wall contact angle at low air and liquid flow rates and it approaches zero at high air and liquid flow rates. The dynamic wall contact angle is a function of both the air and the liquid flow rates as expressed by the non-dimensional parameters that are shown in Fig. 18. An empirical correlation for the results that are presented in Fig. 18 is presented below.

$$\Theta = (\theta_{w,S} - \theta_{w,D})/\theta_{w,S}$$
$$\Theta = 0.5\tanh(10^{-3} Re_f^{0.45} Re_g^{0.6} - 10.25) + 0.5 \quad (4)$$

The simulated film width does not increase significantly beyond the width of the liquid injection region (at the measuring location) and the maximum width is obtained by using a dynamic wall contact angle of zero. As stated earlier the film thickness at the center width of the duct, at the measuring location, is not sensitive to changes in the wall contact angle.

5. Conclusions

Measurements and simulation of three-dimensional shear-driven thin liquid film by turbulent air flow in a duct are reported. The film thickness and width are measured at one streamwise location using an optical technique. The dynamic instabilities that develop at the interface of the thin liquid film made these types of measurements very challenging but provided reasonable results for the average flow characteristics. Results show that increasing the average gas velocity, while maintaining constant liquid flow rate, results in decreasing liquid film thickness but increasing film width. Similarly, increasing liquid flow rate while maintaining constant average gas velocity increases both liquid film thickness and its width. The use of the FLUENT-CFD code along with the Volume of Fluid (VOF) model as a tool for simulating the average characteristics of shear-driven liquid film seem to be a reasonable approach since the simulated and the measured results compared reasonably well with each other. The simulation reveals that the liquid film width decreases if either the surface tension coefficient or the wall contact angle increases without affecting significantly the film thickness. The use of a dynamic wall contact angle improves the comparison between measured and simulated results but establishing analytically the magnitude of the dynamic wall contact angle as a function of flow parameters is still a major challenge. The empirical correlation for the dynamic wall contact angle that was developed in this study can be used to improve comparison between simulated and measured results. Higher gas and liquid flow rates increases the instabilities that develop on the liquid interface (which could not be captured by the steady state simulation) and increases the difference between measured and simulated results.

Acknowledgements

This work was supported in part by a DOE-Basic Energy Sciences Grant No. DE-FG02-03ER46067, and by an NSF Grant No. CTS-0352135.

References

Abe, K., Kondoh, T., Nagano, Y., 1994. A new turbulence model for predicting fluid flow and heat transfer in separating and reattaching flows – I flow field calculations. International Journal of Heat and Mass Transfer 37 (1), 139–151.

Fluent Inc., 2004, Fluent 6.2 User's Guide.

Friedrich, M.A., Lan, H., Drallmeier, J.A., Armaly, B.F., 2006. Characterization of shear-driven liquid film separation and break-up at a sharp corner. In: Proceedings of the 19th Annual Conference on Liquid Atomization and Spray Systems, Toronto, Canada.

Friedrich, M.A., Lan, H., Drallmeier, J.A., Armaly, B.F., 2007. Development of a non-intrusive film thickness measurement technique for dynamic shear-driven thin liquid films. In: Proceedings of the 20th

Annual Conference on Liquid Atomization and Spray Systems, Chicago.

Kelly-Zion, P., Collins, W., Glawe, D., 2004. Application of laser interferometry for transient film thickness measurements. In: Proceedings of ASME Heat Transfer/Fluids Engineering Summer Conference, Charlotte, NC.

Nosoko, T., Mori, Y.H., Nagata, T., 1996. Improved interferometer for measuring unsteady film thickness. Review of Scientific Instruments 67 (8), 2685–2690.

Ohyama, T., Endoh, K., Atsushi, M., Mori, Y.H., 1988. Optical interferometry for measuring instantaneous thickness of transparent solid and liquid films. Review of Scientific Instruments 59 (9), 2018–2022.

Samenfink, W., Elsaber, A., Dullenkopf, K., Wittig, S., 1999. Droplet interaction with shear-driven liquid film: analysis of deposition and secondary droplet characteristics. International Journal of Heat and Fluid Flow 20, 462–469.

Tao, W.Q., 2001. Numerical Heat Transfer. second ed.. Xian Jiaotong Univ. Press, China.

Wang, Y.-P., Wilkinson, G.B., Drallmeier, J.A., 2004. Parametric study on the fuel film breakup of a cold start PFI engine. Experiments in Fluids 37, 385–398.

Wittig, S., Himmelsbach, J., 1992. Motion and evaporation of shear-driven liquid films in turbulent gases. Journal of Engineering for Gas Turbines and Power 114, 395–400.